STRAIN-RATE EFFECTS IN REPLICA SCALE MODEL PENETRATION EXPERIMENTS

By

Charles E. Anderson, Jr.
Scott A. Mullin
Chris J. Kuhlman

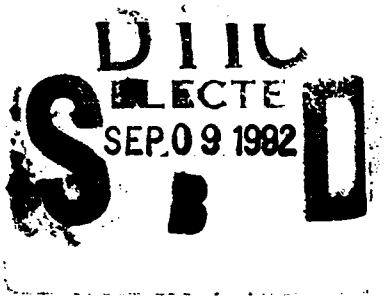

SwRI Report 3593/002
Prepared Under Contract
DE-AC04-90A158770
DAAL3-91-C-0021

Prepared For

Defense Advanced Research Projects Agency
U.S. Army Research Office

August 1992

SOUTHWEST RESEARCH INSTITUTE
SAN ANTONIO HOUSTON
DETROIT WASHINGTON, DC

REPORT DOCUMENTATION PAGE

Form Approved OMB No. 0704-0188 Exp.Date: Jun 30, 1986

REPORT SECURITY CLASSIFICATION: Unclassified

1b. RESTRICTIVE MARKINGS: N/A

SECURITY CLASSIFICATION AUTHORITY:

3. DISTRIBUTION/AVAILABILITY OF REPORT: Approved for Public Release: Distribution Unlimited

DECLASSIFICATION/DOWNGRADING SCHEDULE: N/A

ERFORMING ORGANIZATION REPORT NUMBER(S): SwRI 3593/002

5. MONITORING ORGANIZATION REPORT NUMBER(S):

NAME OF PERFORMING ORGANIZATION: Southwest Research Institute

6b. OFFICE SYMBOL *(If applicable)*:

7a. NAME OF MONITORING ORGANIZATION: U.S. Army Research Office

ADDRESS *(City, State, and ZIP)*: P.O. Drawer 28510, 6220 Culebra Road, San Antonio, TX 78228-0510

7b. ADDRESS *(City, State, and ZIP Code)*: P.O. Box 12211, Research Triangle Park, NC 27709-2211

NAME OF FUNDING/SPONSORING ORGANIZATION: DARPA

8b. OFFICE SYMBOL *(If applicable)*: LSO

9. PROCUREMENT INSTRUMENT IDENTIFICATION NUMBER: DAAL03-91-C-0021

ADDRESS *(City, State, and ZIP)*: 3701 North Fairfax Drive, Arlington, VA 22203-1714

10. SOURCE OF FUNDING NUMBERS

PROGRAM ELEMENT NO.	PROJECT NO.	TASK NO.	WORK UNIT ACCESSION NO.
602618A	AH81	001	–

TITLE *(Include Security Classification)*

) Strain-Rate Effects in Replica Scale Model Penetration Experiments.

PERSONAL AUTHOR(S): Charles E. Anderson, Jr.; Scott A. Mullin; Chris J. Kuhlman

TYPE OF REPORT	13.b TIME COVERED	14. DATE OF REPORT *(Year, Month, Day)*	15. PAGE COUNT
erim	FROM 7/91 TO 4/92	92/8/17	43

SUPPLEMENTARY NOTATION

COSATI CODES			18. SUBJECT TERMS *(Continue on reverse if necessary and identify by block number)*
FIELD	GROUP	SUB-GROUP	Key Words: penetration mechanics; long-rod penetration; numerical simulation; semi-infinite targets; finite-thickness targets; 4340 steel; strain-rate effects; scale modeling; replica modeling; nucleation and growth; damage; damage growth; damage accumulation

ABSTRACT *(Continue on reverse if necessary and identify by block number)*

omputational study has been performed to quantify the effects of strain rate on replica-model (scaled) experiments of penetration d perforation. The impact of a tungsten-alloy long-rod projectile into an armor steel target at 1.5 km/s was investigated. It was nd that over a scale factor of 10, strain-rate effects change the depth of penetration, for semi-infinite targets, and the residual ocity and length of the projectile, for finite-thickness targets, on the order of 5%. Although not modeled explicitly in the present dy, the time-dependence of damage was examined. Damage accumulation is a strong function of absolute time, not scaled e. At homologous times, a smaller scale will have less accumulated damage than a larger scale; therefore, the smaller scale appear stronger, particularly in situations where the details of damage evolution are important.

DISTRIBUTION/AVAILABILITY OF ABSTRACT: ☒ UNCLASSIFIED/UNLIMITED ☐ SAME AS RPT. ☐ DTIC USERS

21. ABSTRACT SECURITY CLASSIFICATION: UNCLASSIFIED

NAME OF RESPONSIBLE INDIVIDUAL: Peter M. Kemmey

22b. TELEPHONE *(Include Area Code)*: (703) 696-2347

22c. OFFICE SYMBOL:

FORM 1473 84 MAR

83 APR edition may be used until exhausted. All other editions are obsolete.

SECURITY CLASSIFICATION OF THIS PAGE

UNCLASSIFIED

Table of Contents

List of Figures

List of Tables

1.0 INTRODUCTION

Scale models are commonly used in experimental investigations. At ordnance velocities, scaled projectiles and targets are generally used to limit the cost of experiments. At higher velocities, since gun systems are kinetic-energy limited, smaller projectile masses must be used to obtain the higher velocities.

Many scaling studies have shown good correlation between the response of the model and the prototype. However, much folklore exists concerning the lack of scaling, and this often leads to a high level of skepticism concerning the validity of scaled experiments. A variety of reasons may exist for the lack of correlation between subscale and full scale tests. These reasons could include improper scale modeling analysis, lack of understanding or neglect of important parameters, failure to construct models properly, failure to test under the proper ("scaled") conditions, lack of attention to material selection, etc. In addition, there can be terms in the model analysis that cannot be held constant between the model and the prototype. These items, acting along or in concert, could result in dissimilar responses.

Strain rate is a term that cannot be kept constant between a replica-scaled model and the prototype in penetration problems. We have used numerical simulations to quantify the expected magnitude of strain-rate effects on the response of penetration into semi-infinite and finite-thickness steel targets impacted by tungsten long-rod projectiles at a typical ordnance velocity of 1.5 km/s. In addition to quantifying strain-rate effects, we also compare and contrast the penetration time histories of semi-infinite and finite-thickness targets.

2.0 MODEL ANALYSIS

2.1 Model Parameters

The analysis begins with the selection of the important terms for the problem. Figure 1 depicts an idealized impact condition; we have elected to examine normal impact for the purposes of this study. The impact velocity and the geometry define the initial impact conditions. If the target is sufficiently thick, there will be no perforation and the measure of ballistic performance is the depth of penetration. Otherwise, the target plate is perforated, and the remnant projectile is characterized by some residual mass and velocity.

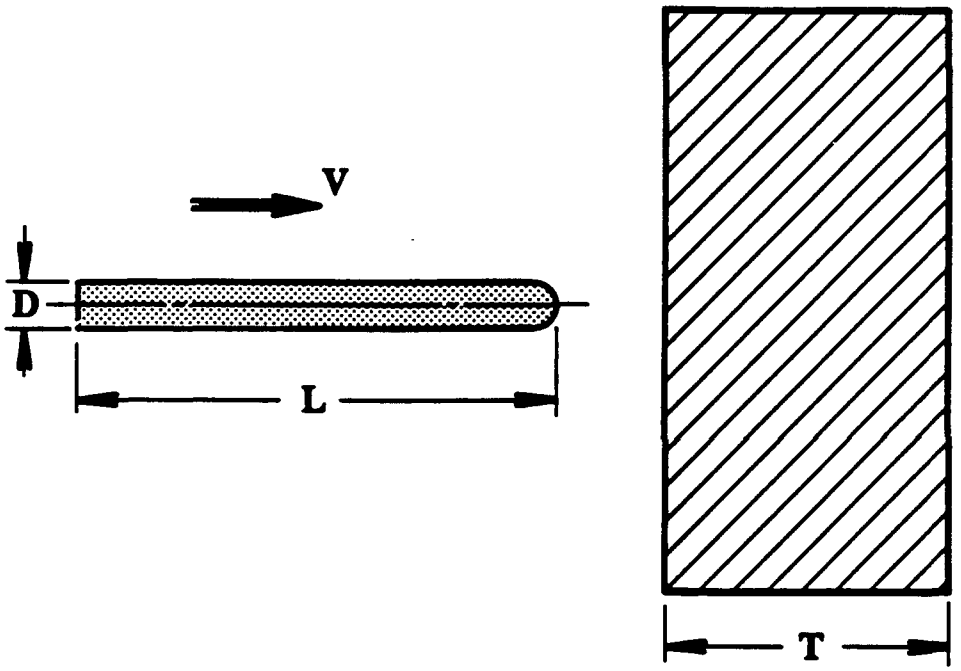

Figure 1. Depiction of Initial Conditions for the Impact Model

Table 1 lists the projectile and target parameters. Typical units are shown for each parameter, along with the fundamental units of mass (M), length (L), time (τ), and temperature (θ). Some of these parameters are also shown on Fig. 1, which depicts the geometry. The projectile is considered to be a constant diameter long rod with a hemispherical nose. The geometrical terms necessary to describe it are the diameter and the length. The density and impact velocity describe the inertial properties. The constitutive behavior is characterized by the flow stress and equivalent plastic strain of the projectile material. The specific heat is a measure of the ability to absorb heat. Also listed in Table 1 are the target parameters. The target is considered to be homogeneous and of uniform thickness. The constitutive parameters for the target plates are similar to those of the projectile,

with the exception of the addition of fracture toughness. Fracture toughness was included as a descriptor that might help account for failure characteristics of the rear of the target during perforation. The subscripts "p" and "t" in Table 1 refer to the projectile and target, respectively.

The response parameters that generally are of interest are listed in Table 2; some of these parameters are shown in Fig. 2. The left-hand figure provides a schematic for a semi-infinite target, and the right-hand figure depicts a finite-thickness target. Most of these response parameters can be measured directly in experiments, and thus they provide a means for comparing and evaluating the similarity of the different scale model sizes. These parameters include the residual length, velocity, and mass of the projectile. For the semi-infinite target, the residual velocity is not appropriate; instead, the depth of penetration is the parameter of merit. Strain rate and temperature are generally not measured directly, but are used to help understand the dynamic conditions that occur in models of different sizes. The time appears as a response variable since many of the parameters can be functions of time.

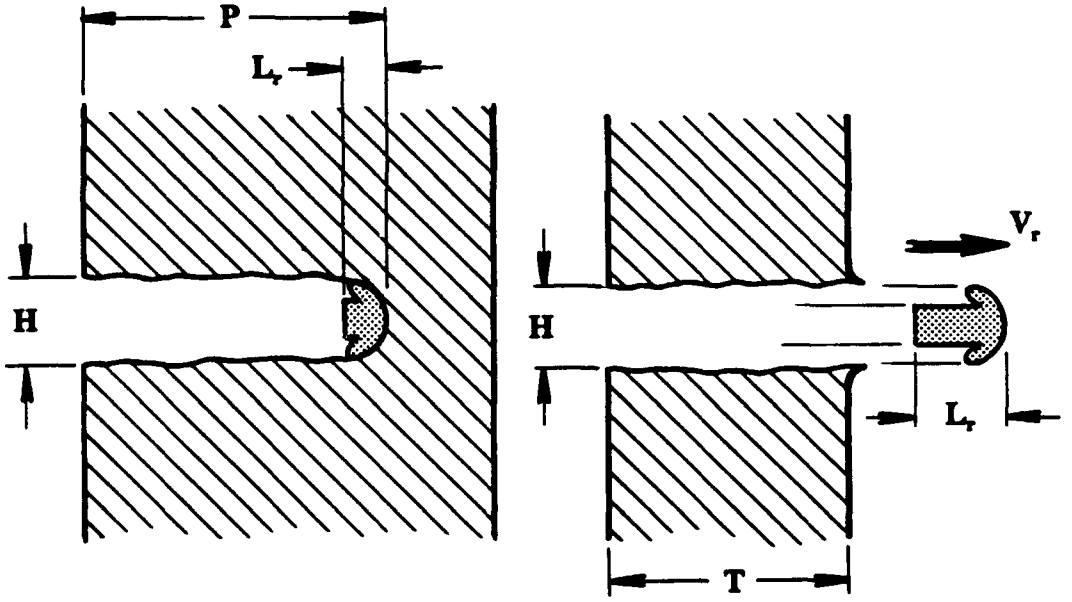

(a) Semi-Infinite Target (b) Finite-Thickness Target

Figure 2. Impact Model: Response

2.2 Pi Terms

The parameters shown in Tables 1 and 2 can be formed into nondimensional terms, referred to as Pi terms, by applying the Buckingham Pi Theorem [1]. The methodology is rather straightforward and will not be described here. One set of Pi terms is shown in Table 3. They are grouped into major categories, such as geometric and material characterizations, and terms that

Table 1. Projectile and Target Parameters

Parameter	Description	Typical Units	Fundamental Units
D	projectile diameter	(m)	L
L	projectile length	(m)	L
ρ_p	projectile density	(kg/m^3)	M/L^3
σ_p	projectile flow stress	(Pa)	M/τ^2L
ε_p	equivalent plastic strain of projectile	(-)	-
c_p	projectile specific heat	(J/kg-K)	L^2/$\tau^2\theta$
ρ_t	target density	(kg/m^3)	M/L^3
σ_t	target flow stress	(Pa)	M/τ^2L
ε_t	equivalent plastic strain of target	(-)	-
c_t	target specific heat	(J/kg-K)	L^2/$\tau^2\theta$
T	target thickness	(m)	L
K_t	target fracture toughness	(Pa$\sqrt{m}$)	M/τ^2L$^{1/2}$
V	impact velocity	(m/s)	L/τ

Table 2. Response Parameters

Parameter	Description	Typical Units	Fundamental Units
P	penetration depth	(m)	L
H	hole diameter in target	(m)	L
V_r	projectile residual velocity	(m/s)	L/τ
L_r	projectile residual length	(m)	L
M_r	projectile residual mass	(kg)	M
θ_p	projectile temperature	(K)	θ
θ_t	target temperature	(K)	θ
$\dot{\varepsilon}$	strain rate	s^{-1}	1/τ
τ	time	(s)	τ

contain response parameters. In Table 3, we have elected to represent the constitutive strength of each material as the product of the flow stress times the equivalent plastic strain ($\sigma_p\varepsilon_p$ or $\sigma_t\varepsilon_t$), which can be viewed as representative of the ability of the material to absorb energy in the form elastic-plastic work. These Pi terms do not represent a unique set; other Pi terms may be formed through combination (multiplying, dividing, raising to a power) of existing terms.

Table 3. Pi Terms for Penetration Problem

Geometric	Material Characterization	Response
$\pi_1 = L/D$	$\pi_3 = \sigma_p\varepsilon_p/\sigma_t\varepsilon_t$	$\pi_9 = V_r/V$
$\pi_2 = T/D$	$\pi_4 = V^2\rho_p/\sigma_t\varepsilon_t$	$\pi_{10} = L_r/L$
	$\pi_5 = K_t/\sigma_t\varepsilon_t T^{1/2}$	$\pi_{11} = M_r/\rho_p D^3$
	$\pi_6 = \rho_p/\rho_t$	$\pi_{12} = H/D$
	$\pi_7 = \varepsilon_p$	$\pi_{13} = P/L$
	$\pi_8 = \varepsilon_t$	$\pi_{14} = \dot{\varepsilon}D/V$
		$\pi_{15} = \tau V/D$
		$\pi_{16} = \rho_t c_t\theta_t/\sigma_t\varepsilon_t$
		$\pi_{17} = \rho_p c_p\theta_p/\sigma_p\varepsilon_p$
		$\pi_{18} = \theta_t/\theta_p$

2.3 Similarity and Geometric Scale Factor

The Pi terms shown in Table 3 represent ratios or balances of the parameters involved in the problem. By the principles of similitude modeling, *when the values of the geometric and material characterization terms are kept invariant between two different experiments, the experiments will display "similar" response.* In other words, the values of the response Pi terms will be equal between the experiments. It is important to realize that the magnitude of each individual parameter does not have to be equal, but rather the magnitude of the Pi terms must be equal. The practical advantage of these Pi terms is in the ability of one scale size to produce response data applicable to other sizes. For example, the material characterization Pi terms serve to balance stress, mass, or energy between different scale experiments. The Pi term $[\rho_p V^2/\sigma_t\varepsilon_t]$ represents a balance between the kinetic energy of the projectile and the strain energy absorbed by the target; the term $[\rho_p/\rho_t]$ serves as a measure of the density (inertia) mismatch between the target and the projectile. The Pi term $[\rho_t c_t\theta_t/\sigma_t\varepsilon_t]$

represents the ratio of internal (thermal) energy to plastic work. Plastic work increases the bulk temperature of the material, which can lead to thermal softening. Since there is little time for heat conduction, thermal conductivity effects have been ignored in this analysis.

There are several ways to satisfy the requirements imposed by the Pi terms to develop a model of a physical system (referred to as the prototype). The approach used in this effort, and generally the most common approach, is to develop a replica model. A replica model is one in which the same materials are used in the model as the prototype, with the only difference being geometric size. The model is constructed so as to mimic the arrangement of the prototype, with corresponding materials at corresponding locations. The model is said to be homologous (corresponding, but not necessarily equal) to the prototype.

The size of a replica model relative to the prototype is described by the geometric scale factor, denoted by λ. The λ in this work will represent subscale sizes, such as 1/10. By fixing the geometric scale factor, the values of all the other parameters in the model can be determined in terms of λ by using the Pi terms of Table 3. For example, to maintain the value of the Pi term L/D equal in a model and prototype, both the length (L) and the diameter (D) of the model have to be sized such that they are λ times the prototype values. This will be true of all linear geometric quantities in the model. The Pi term $[\rho_p V^2/\sigma_t\varepsilon_t]$ is used to determine the appropriate impact velocity for the subscale model experiment. Since we are assuming a replica model, both ρ_p and $(\sigma_t\varepsilon_t)$ are equal in model and prototype. Thus, keeping $[\rho_p V^2/\sigma_t\varepsilon_t]$ invariant requires the same velocity in the model as for the prototype. Following a similar procedure for all the Pi terms develops a model law. A model law is a set of scale factors for all parameters involved in the model analysis that satisfy the requirements imposed by the Pi terms. Table 4 provides the scale factors for the parameters involved in this model analysis.

2.4 Replica Model Issues

The assumption of a replica model and the model law presented in Table 4 contain some inherent issues that may lead to distortions in the ability of subscale models to reproduce full-scale results. For the model to reproduce the prototype response, all Pi terms must remain invariant. Sometimes, the model law results in conflicting requirements on the Pi terms, thereby making it impossible to keep all Pi terms invariant simultaneously. Then the question becomes: How much distortion results between the responses of the prototype and model because of Pi term(s) not being invariant? Several issues are discussed below.

The assumption of a replica model requires that the subscale models have the same material properties, e.g., density and strength, as the prototype. This is trivial for the density, but may be difficult for strength for two reasons. The first is that manufacturing processes will lead to different

Table 4. Model Law for Replica Model

Parameter	Scale Factor
Geometric Lengths	λ
Strength ($\sigma \cdot \varepsilon$)	1.0
Velocity	1.0
Fracture toughness	$\sqrt{\lambda}$
Density	1.0
Mass	λ^3
Pressure	1.0
Stress	1.0
Temperature	1.0
Strain Rate	$1/\lambda$
Time	λ

strengths for different thicknesses of plates of the same material. Generally, thinner plates are stronger due to increased amounts of cold working or other manufacturing processes. A similar condition may occur for the projectiles. This discrepancy can be overcome through careful selection and manufacturing of the projectile and target pieces. For example, all target plates can be cut from the same stock items, with care taken to insure that the target centerline corresponds for all tests.

The second issue related to strength involves the effects of strain rate. The model law in Table 4 indicates that the strain rate in a subscale model will be higher than that in a larger prototype:

$$\dot{\varepsilon}_{Model} = \lambda^{-1}\dot{\varepsilon}_{Prototype}$$

For $\lambda = 1/10$, the following relationship exists between the strain rates for the model and prototype:

$$\dot{\varepsilon}_{Model} = 10\dot{\varepsilon}_{Prototype}$$

Pi term 14 [$\dot{\varepsilon}D/V$] maintains the same value for model and prototype, as required, when the strain rate increases in the model. The important point is not that the strain rate increases, but the effect this may have upon the model response. It is known that some materials exhibit increased strength as strain rate increases. Thus, the subscale target and projectile may exhibit greater resistance to plastic flow than the larger prototype. Pi terms that depend upon the flow stress—Pi terms 3, 4, 5, 16, and 17—will be distorted. The objective of this study is to quantify the effect of these distortions.

Another material property issue that results from the model law in Table 4 is the scaling of fracture toughness. The replica model law states that the fracture toughness should decrease as the size is made smaller, whereas for most materials, measured values of fracture toughness increase for smaller specimens. Thus, there is the potential for failure processes not being similar in the model and the prototype. The focus of this study, however, is on strain-rate effects.

In general, it is reasonable to state that if the response is weakly dependent on some parameter, then a distortion in the associated Pi terms will probably not appreciably affect the response. Conversely, if the target and projectile response is strongly dependent upon a parameter that cannot remain invariant, then this could cause nonscaling of results.

3.0 INVESTIGATION OF STRAIN-RATE EFFECT

3.1 Analysis Methodology

The three-dimensional Eulerian wave propagation computer program, CTH [2], was used to perform the numerical experiments to investigate the magnitude of strain-rate effects. The 2-D cylindrically symmetric option was used for the computations. CTH uses a van Leer algorithm for second-order accurate advection that has been generalized to account for a non-uniform and finite grid, and multiple materials. Further, CTH has an advanced material interface algorithm for the treatment of mixed cells [2]. Also, CTH has been modified to account for more realistic constitutive treatment of material response by allowing the flow stress to be functions of strain and strain rate [3-4].

Projectile and target materials typically used in armor penetration experiments were selected for the numerical simulations to provide a realistic quantification of the strain-rate effect. The target was considered to be 4340 steel with a hardness of Rockwell C 30. The tungsten-alloy, long-rod projectile was modeled with a length-to-diameter (*L/D*) ratio of 12. The impact velocity was 1.5 km/s. The prototype projectile (full scale) had a diameter of 2.54 cm. A scale factor of 1/10 was selected for the study. The term "prototype" will be used in reference to the results for the 2.54-cm diameter projectile, and the term "model" will be used in reference to the results for the 2.54-mm diameter projectile.

Square zoning (with seven zones across the radius of the projectile) was used in the interaction region. All geometric dimensions were exactly 1/10 smaller in the "scaled" calculation; therefore, to achieve the same numerical resolution, the cell dimension of the computational grid was 1/10 the size of the full scale computation (that is, seven zones were used across both the full scale and the 1/10 scale projectiles). The Courant stability criterion limits the integration time step; thus the computational time steps also differed by a factor of ten between the two computations. The total computation (CPU) times were virtually identical for the two scale sizes.

The constitutive response for 4340 steel was represented by the Johnson-Cook model [5]:

$$\sigma_f = 792\,[1 + 0.644\varepsilon_f^{0.26}]\,[1 + 0.014 \ln \dot{\varepsilon}_f^{*}]\,[1 - T_f^{*1.03}] \qquad (1)$$

where σ_f is the von Mises effective flow stress (in MPa), 792 MPa is the quasi-static yield stress, ε_f is the equivalent plastic strain, $\dot{\varepsilon}_f^{*} = \dot{\varepsilon}_f/\dot{\varepsilon}_o$ is the dimensionless plastic strain rate ($\dot{\varepsilon}_o = 1.0\,s^{-1}$), and T_f^{*} is the homologous temperature. Equation (1) was used to obtain the stress-strain behavior of 4340 steel for three strain rates: 10^0, 10^3 and 10^5 s^{-1}. There are two sets of curves shown in Fig. 3a.

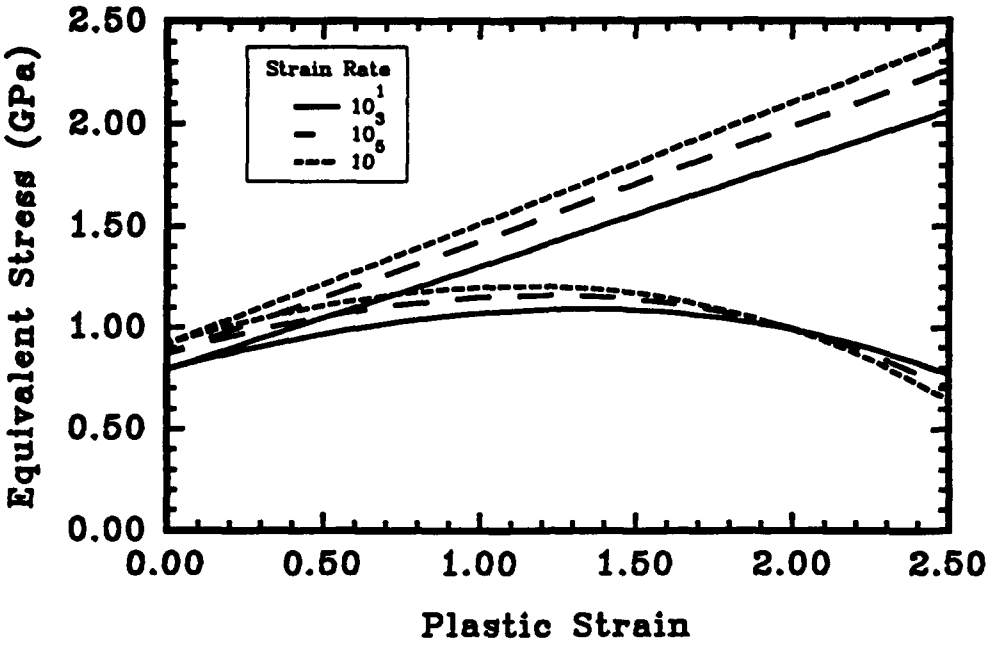

(a) 4340 Steel (R_c30)

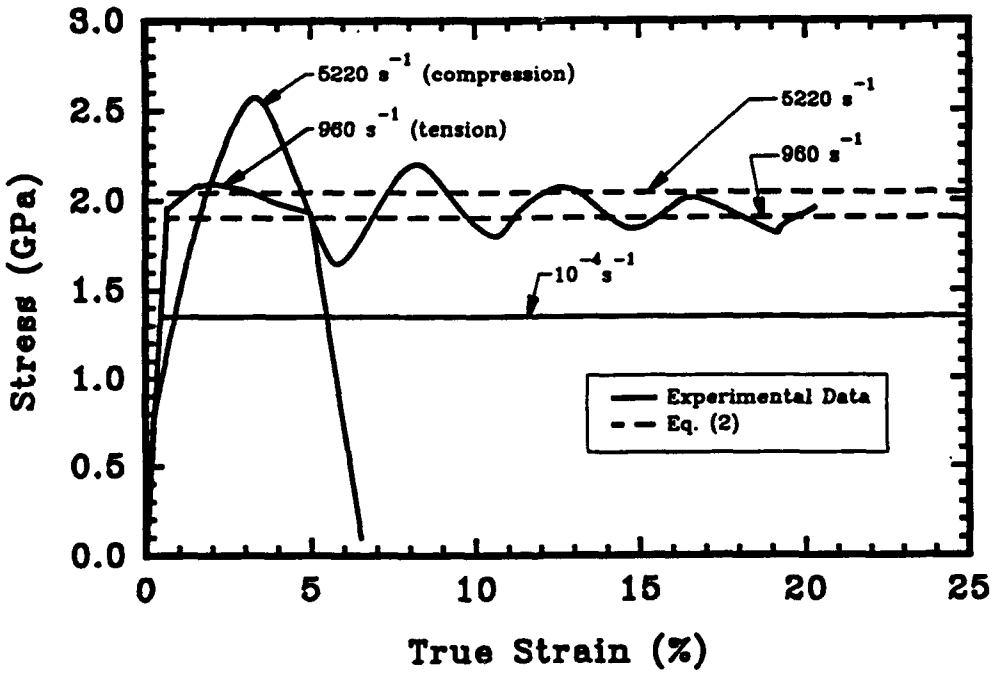

(b) Tungsten Alloy (X27-C)

Figure 3. Constitutive Response

The upper set depicts the effect of strain rate and work hardening only; the lower set of curves shows both of these effects plus thermal softening, assuming that all plastic work goes into thermal heating.

The plastic work is given by the area under the stress-strain curve. For the same plastic strain, thermal softening is virtually unaffected by strain rate effects, particularly since it is the natural logarithm of the strain rate that appears in Eq. (1). Therefore, the temperatures will be nearly the same at homologous locations and time. Thus, Pi term 16 can be considered to be essentially invariant between scale sizes; the model law, given in Table 4, indicates that the scale factor for temperature is 1.0. (As stated earlier, it has been assumed that the time scales are sufficiently short to preclude heat conduction effects. In problems where heat conduction is important, temperature scaling will be distorted at homologous times.)

We have examined a number of tungsten (90-93% by weight) alloys, and the stress-strain response can be modeled using an expression of the form [6]:

$$\sigma_p = 1350\,[(1+\beta\varepsilon_p)^n + 0.06\ln\dot{\varepsilon}_p^*] \qquad (2)$$

In particular, the work hardening and strain rate effects are found to be "independent" in that the strain-rate effect does not alter the slope of the strain-hardening curve. For the particular tungsten alloy used for these experiments, the initial yield stress is strain-rate dependent, but there is little work hardening (Fig. 3b), so β and n are zero.

3.2 Semi-Infinite Targets

Preliminary Computations: Strain-Rate Effects Set to Zero. Computations were performed initially to insure that the computational methodology was scale independent. The projectile and target materials were modeled considering only strain-hardening effects, i.e., the strain rate coefficients in Eqs. (1-2) were set to zero.[1] Strain rate and equivalent plastic strain contours are plotted at homologous times in Fig. 4. The results for the prototype are given in the left figure, and the results for the model are given in the right figure. The dimensions on the lower borders of the plots provide the spatial extent, which differs by the geometric scale factor of 10 for the two figures. The model law summarized in Table 4 shows that time scales as the geometric scale factor; note that the homologous time for the model is 1/10 that of the prototype.

1. The materials were modeled initially as elastic, perfectly plastic, and the results for the prototype and model computations compared. The conclusions are identical to those of the more general case that includes strain hardening.

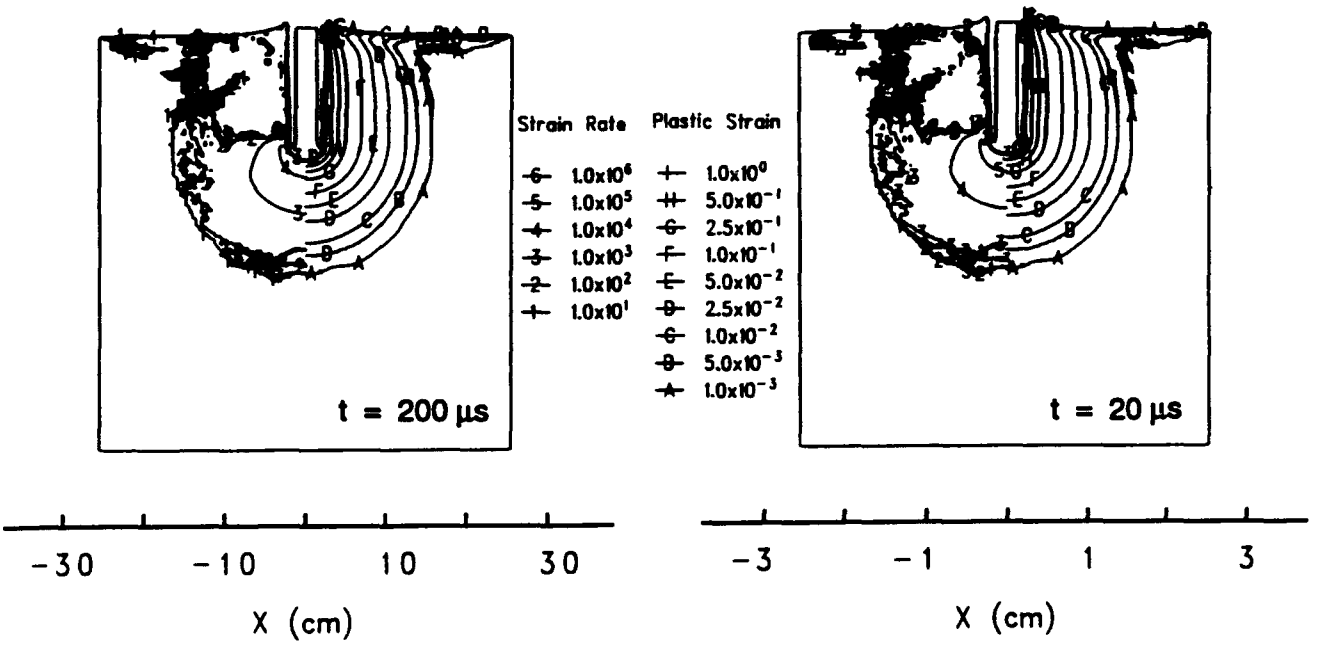

(a) Full-Scale Target ($\lambda = 1$; t = 200 μs) **(b) Tenth-Scale Target ($\lambda = 1/10$, t = 20 μs)**

Figure 4. Strain Rate and Equivalent Plastic Strain Contours: Semi-Infinite Target

Strain rate contours are depicted to the left of the centerline, and plastic strain contours are shown on the right in the two figures. If the model results are overlaid on the prototype results, the contour lines overlay exactly, except that the strain rate is a factor of 10 higher for the model. Although the strain rates are higher in the model, the total plastic strains are identical at the homologous locations, a consequence of the fact that the time scales as the geometric scale factor, i.e.:

$$\varepsilon^p_{Model} = (\dot{\varepsilon}^p \tau)_{Model} = (\dot{\varepsilon}^p_{Prototype} / \lambda) \cdot (\lambda \tau_{Prototype}) = (\dot{\varepsilon}^p \tau)_{Prototype} = \varepsilon^p_{Prototype} \qquad (3)$$

where the superscript "p" is a reminder that ε represents the equivalent plastic strain. These observations are in agreement with the model law summarized in Table 4. Although the strain rates are higher by a factor of 10 in the model than in the prototype, the stresses, depth of penetration, etc., are not affected since the material response (constitutive) model used for these calculations is rate independent. Comparisons were made between the velocity, pressure, and stress profiles, velocity-time and pressure-time histories, etc., and the computational results were identical after accounting for geometric scale and time.

Therefore, it was concluded that the computer program does not have a rate-sensitive numerical formulation. This might seem to be an obvious conclusion at first glance. However, shock wave propagation computer codes use artificial viscosity as a dissipative mechanism to dampen numerical oscillations behind shock fronts [7]. The artificial viscosity is written in terms of a strain rate, $\partial v/\partial x$, which would imply a rate-sensitive effect. However, the numerical implementation of the artificial viscosity is such as to make it independent of the mesh size, i.e., the shock is smeared over 5 to 7 computational zones. Since the number of zones was kept the same in the prototype and model computations, artificial viscosity does not affect the scaling.

Strain-Rate Dependent Modeling. Calculations were next performed with the full-up constitutive model of Eqs. (1) and (2). The penetration (nose) and tail velocities of the projectile, along the centerline, are shown in Fig. 5 for the prototype and model calculations. The time axis is for the prototype calculation; the homologous times for the model calculation are a factor of 10 less. The penetration and tail velocities as a function of penetration depth are shown in Fig. 6; similar to Fig. 5, the depth of penetration—the abscissa—is for the prototype projectile, and the values are one-tenth for the model.

The larger strain rate in the model calculations results in both a stronger target and a stronger projectile. However, studies have shown that the depth of penetration is very sensitive to the strength of the target, but quite insensitive to projectile strength [6,8]. It is observed that the scaled penetrator does not go as deep as the prototype penetrator, and because it does not go as deep, penetration is completed slightly sooner (in comparing homologous times). The homologous total penetration times differ by approximately 3%.

The normalized depth of penetration P/L provides a method for directly comparing scale effects. The prototype P/L is 0.804, and the model P/L is 0.763; the normalized depth of penetration is approximately 5% less for the model than the prototype. This is an interesting finding, with consequences concerning penetration studies performed with replica models. A very reasonable approximation is that the strain-rate effect is linear over the factor of 10 in scale size, since the strain-rate effect for the depth of penetration is only 5%. The results for long-rod penetration into semi-infinite targets are commonly displayed as normalized depth of penetration versus impact velocity. By necessity, scaled projectiles have to be used at very high velocities since gun systems are kinetic energy limited. Thus, if the interest is over a large velocity range, the results from different scale sizes are often plotted on the same graph. Experimental scatter for well-controlled experiments (at the same scale size) for tungsten-alloy projectiles impacting semi-infinite armor steel is ±5% [6]. Geometric scale factors are generally on the order of 4 or 5. A difference in a

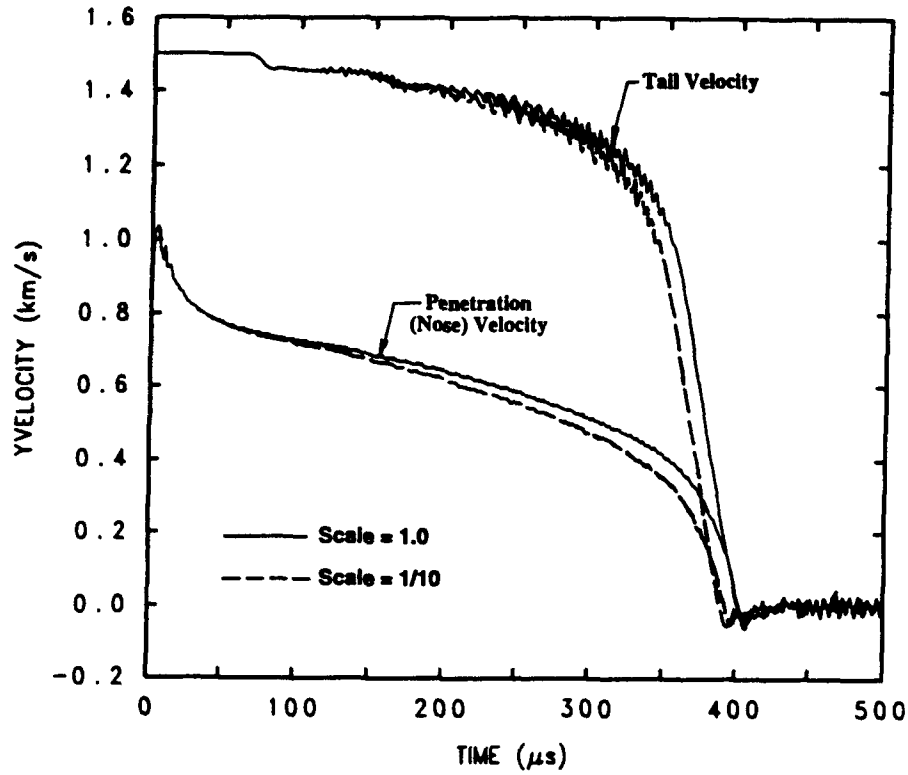

Figure 5. Centerline Penetration and Tail Velocities versus Time: Semi-Infinite Targets

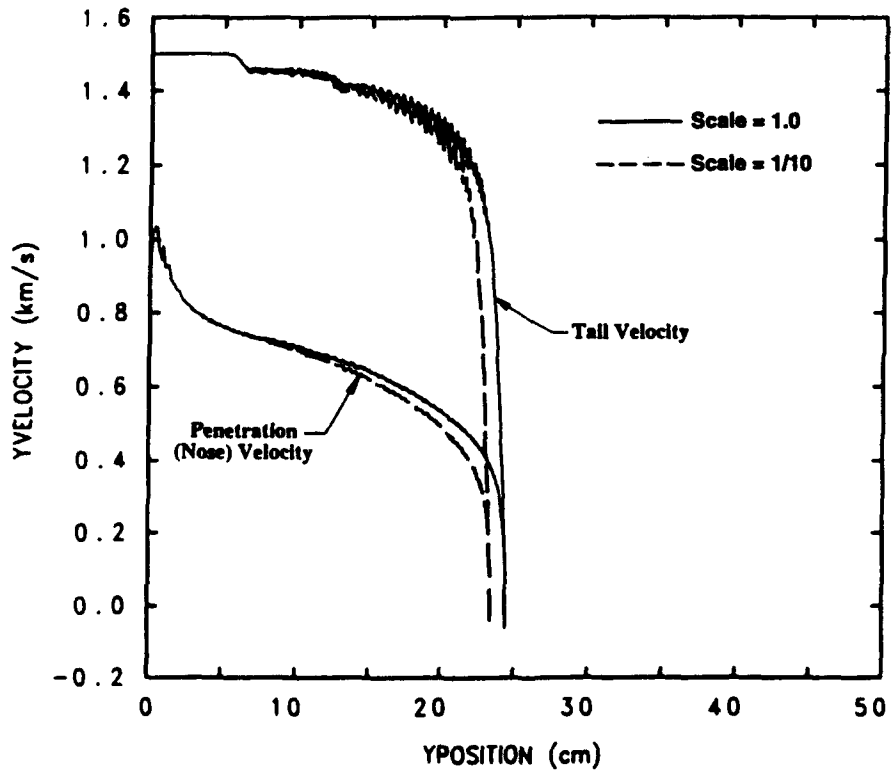

Figure 6. Centerline Penetration and Tail Velocities versus Penetration Depth: Semi-Infinite Targets

scale factor of five between two projectiles would lead to only a 2.5% difference in the normalized depths of penetration; this lies well inside experimental scatter. Thus, the computational results here explain the general lack of observed scale dependency in depth-of-penetration studies.[2]

The positions versus time for the nose and tail of the projectile are shown in Fig. 7. As already indicated in Fig. 6, the model projectile does not go as deep as the prototype. The instantaneous length of the projectiles is given by the distance between the nose and the tail; the residual length of the model projectile is greater than that of the prototype projectile by approximately 5%. A caution here is that there is uncertainty in the results of Eulerian codes in mixed cells, and it is in mixed cells near the end of penetration that the projectile is transitioning from eroding to rigid-body behavior. Nevertheless, the computations are in agreement with experimental observations that indicate the residual length of a projectile tends to increase with increased projectile strength.

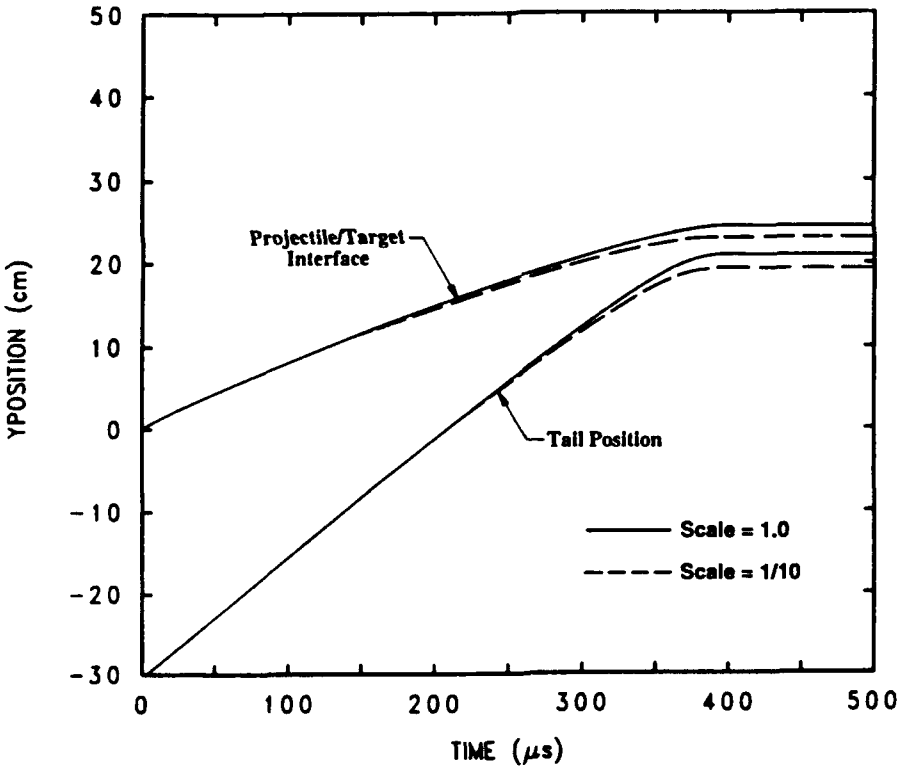

Figure 7. Centerline Penetration (Interface) and Tail Positions versus Time: Semi-Infinite Targets

2. It is well-known, however, that *P/L* is sensitive to heat treating or alloying of the target material, and projectile *L/D*.

The above remarks apply specifically to tungsten-alloy projectiles impacting armor-type steels. We can conclude that over a scale factor of ten, rate effects cannot typically be separated from experimental variability. A larger effect would be observed if a more strain-rate sensitive target material were to be used. For example, mild steels can be fairly strain-rate sensitive. Further, because the depth of penetration is a function of target strength, a mild steel target is a more "sensitive" gage in that the projectile will penetrate further than in a hard steel target. Strain-rate effects would then be more noticeable.

3.3 Finite-Thickness Targets

Contrast of the Penetration Histories of Semi-Infinite and Finite-Thickness Targets. The computational study permits us to contrast the penetration history of a finite-thickness target against that of a semi-infinite target. For this comparison, it is only necessary to examine one of the scale sizes; we have chosen to use the full-scale results for the comparison. The target was defined to be 7 projectile diameters thick. This target is sufficiently thick so that the projectile achieves quasi-steady-state penetration before the rear surface of the target influences the penetration history.

Figure 8 shows the penetration and tail velocities as a function of time for both the finite-thickness and semi-infinite targets. The penetration histories are identical until approximately 100 μs, at which point the two penetration velocities begin to diverge (the response of the tails of the projectile remain identical until late in the penetration process). It is instructive to examine the plastic strain contours at various times, and in particular, at times where the penetration velocity-versus-time curve has a noticeable change in slope. A contour plot exists for each of the times denoted by an arrow in Fig. 8, and labeled *a* through *f* in both Figs. 8 and 9. At 50 μs, except for possibly some inconsequential elastic waves, the projectile "sees" a semi-infinite target. However, at 100 μs, the rear of the target has seen 1% plastic strain, i.e., it is just starting to bulge. Figure 10 shows the pressure versus time for both the finite-thickness and semi-infinite targets. From Figs. 9 and 10, it is concluded that the pressure begins to decrease due to the lack of confinement (as compared to the semi-infinite target) when the plastic zone reaches the rear surface. The penetration velocity remains relatively constant between 100 μs and 200 μs during bulge formation and growth. At approximately 200 μs, using the terminology of Ravid and Bodner [9], the bulge ceases to grow radially and instead is displaced axially, referred to as bulge advancement. The target material in the sides of the bulge continues to strain and "thin" until target perforation, distinguished by the fact that the nose velocity becomes "flat," at approximately 335 μs. The nose and tail of the projectile do not have the same velocity at the time of perforation since the nose has

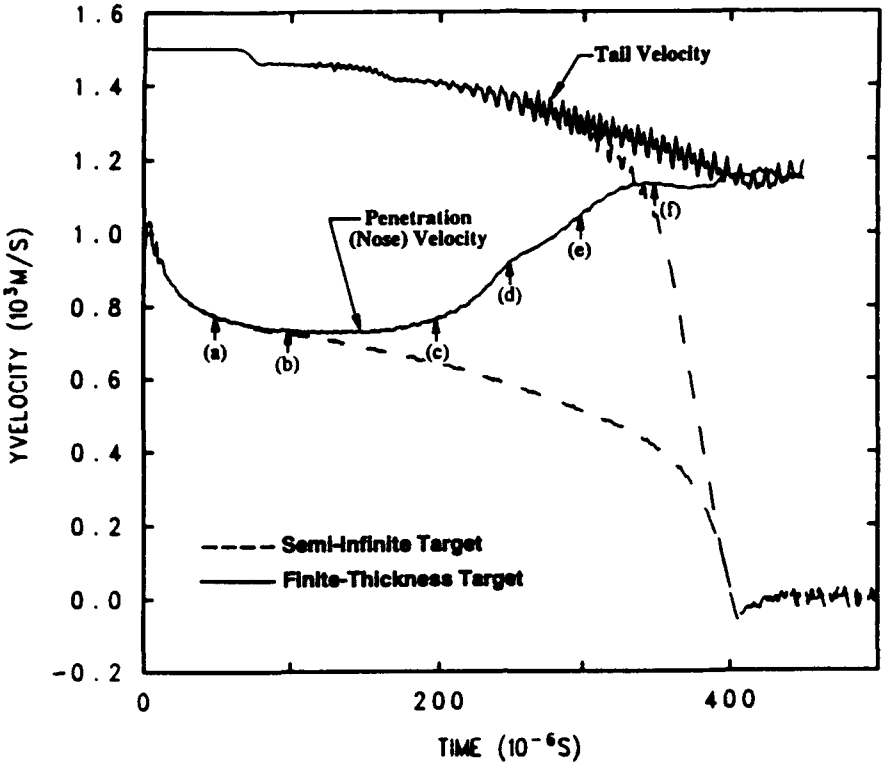

Figure 8. Centerline Nose and Tail Velocities versus Time: Semi-Infinite and Finite-Thickness Targets

been encountering some resistance to penetration. It takes several longitudinal elastic wave transits within the projectile before the velocity is equilibrated at 400 μs; this will be discussed in more detail a little later.

The penetration and tail velocities for the semi-infinite and finite-thickness targets plotted versus the depth of penetration are displayed in Fig. 11. Vertical lines, separated by one projectile diameter, are drawn on the figure. Several conclusions can be drawn from this figure. The effect of the shock phase lasts for approximately 1.5 projectile diameters (1.5 *D*) of penetration for the impact conditions studied here, after which the projectile enters the quasi-steady-state penetration phase. The fact that the target is finite affects penetration when the projectile is approximately 4.5 *D* (100 μs in Fig. 8) from the rear surface. The target material continues to offer resistance to penetration/perforation for quite some time after the projectile nose has passed the original rear surface (230 μs in Fig. 8); however, there is an inflection in the slope of the penetration velocity when the projectile nose has gone approximately 0.75 *D* past the original position of the rear surface. This point corresponds to a time of 250 μs in Fig. 8. After this point, the bulge is "thinning" as

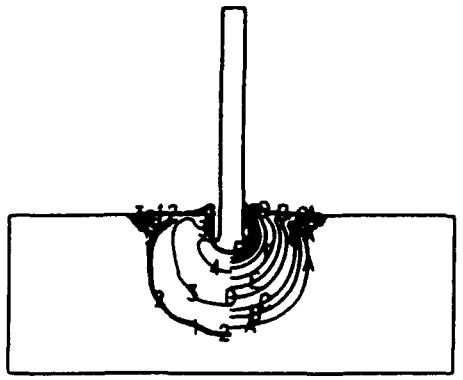

(a) t = 50 μs

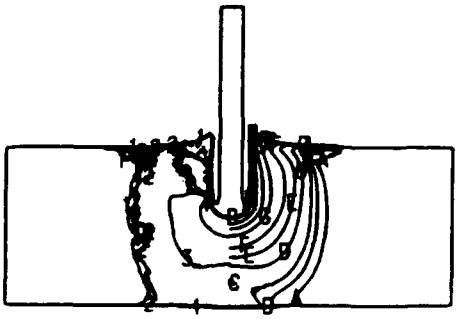

(b) t = 100 μs

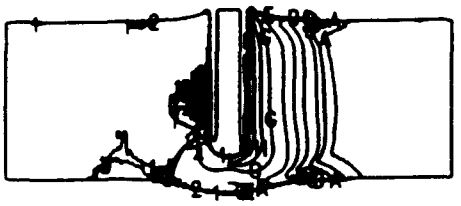

(c) t = 200 μs

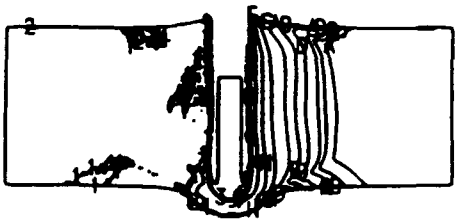

(d) t = 250 μs

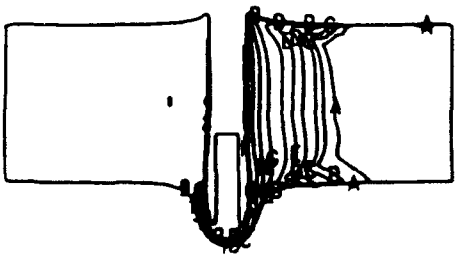

(e) t = 300 μs

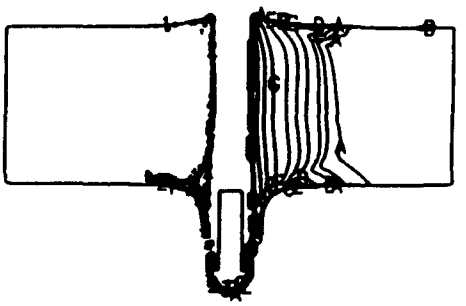

(f) t = 350 μs

Figure 9. Strain Rate and Equivalent Plastic Strain Contours: Finite Thickness Target

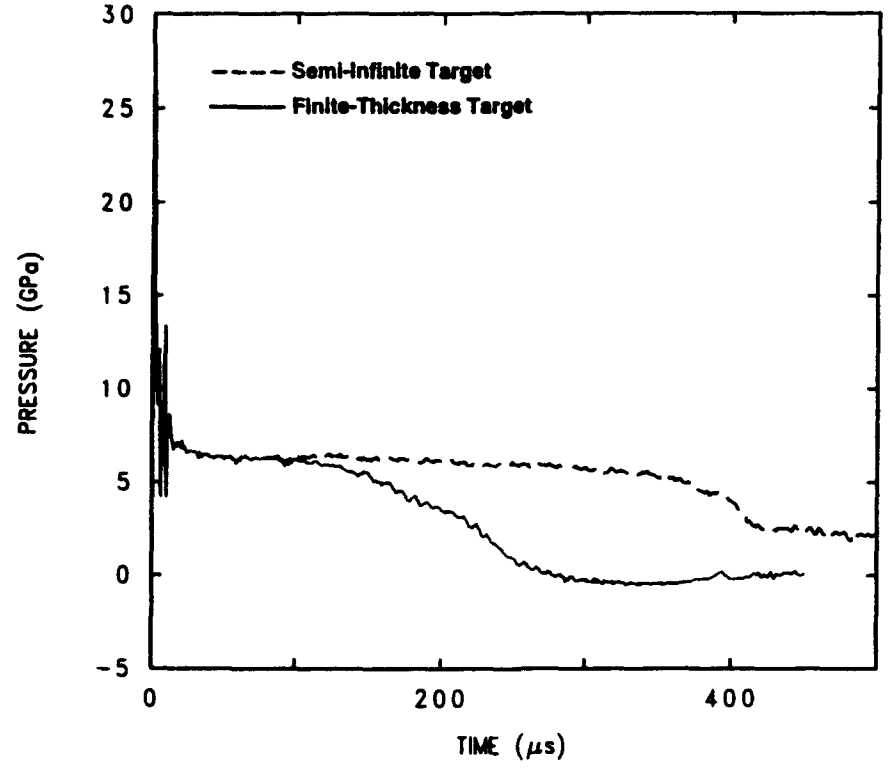

Figure 10. Interface (Centerline) Pressure versus Time: Semi-Infinite and Finite-Thickness Targets

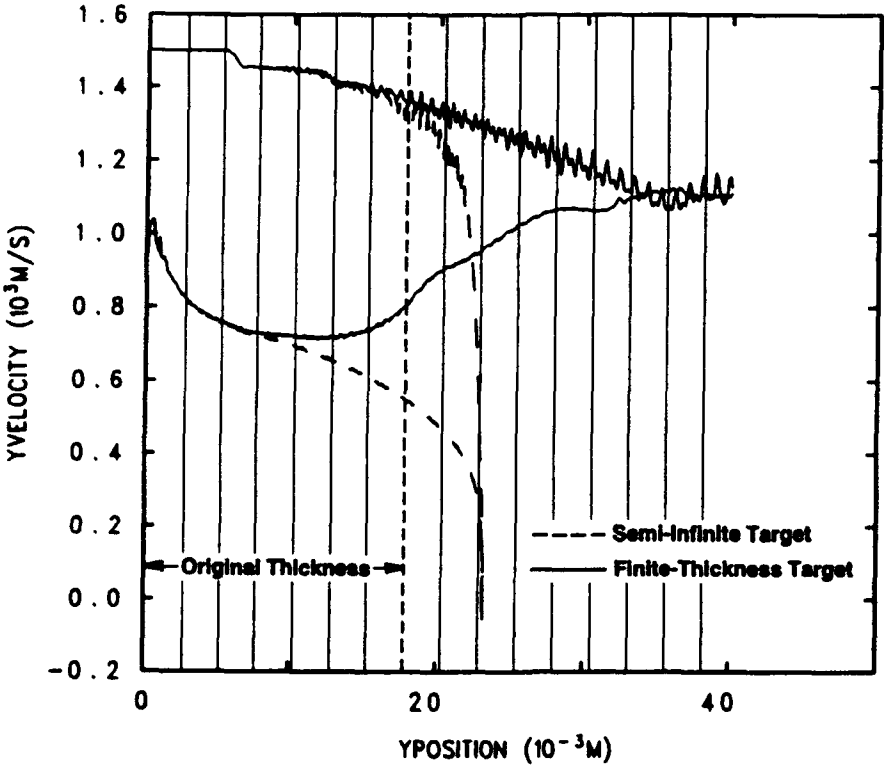

Figure 11. Centerline Penetration and Tail Velocities versus Depth of Penetration: Semi-Infinite and Finite-Thickness Targets

opposed to advancing. According to the computational results, the target influences "penetration" 4 *D* (335 μs in Fig. 8) past the original rear surface; however, this is a consequence of the treatment of failure for this computational model.

The fracture algorithm in CTH is a simple, heuristic tensile stress model. An input fracture pressure (mean stress) denotes the tensile pressure at which fracture will occur. If the pressure is more tensile than the fracture pressure, then the void volume in the cell is increased to relax the tensile pressure. In the computation here, the target is considered to be infinitely ductile. The material thins due to the stretching until sufficient void is present to "break" the material. More realistically, the target material will fail after some finite amount of strain. For this particular computation, this "detail" does not invalidate most of the conclusions. This is largely because the penetration velocity is rapidly increasing after 250 μs, and therefore, only a little projectile erosion occurs between 250 μs and breakout. This is evident in Fig. 12, which depicts the position of the nose and tail of the projectile versus time (and provides a comparison of the projectile response for the semi-infinite and finite-thickness targets). The distance between the nose and tail at any instant in time gives the length of the projectile.

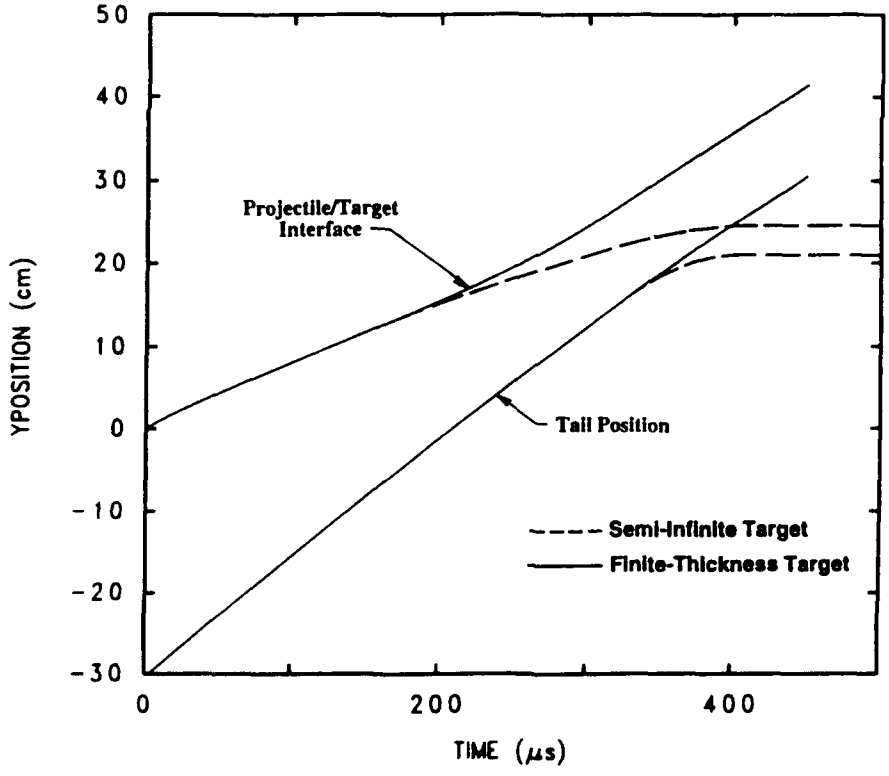

Figure 12. Centerline Penetration (Interface) and Tail Positions versus Time: Semi-Infinite and Finite-Thickness Targets

If a more realistic failure criterion had been used, the remnant projectile would have been slightly longer, and the residual velocity would have been correspondingly higher. To investigate the potential for failure more closely, we examined the contours of equivalent plastic strain in the bulge region at several time increments. At 225 μs, plastic strains between 25% and 50% exist within the bulge region; at 250 μs, all the region has undergone 50% plastic strain; and by 275 μs, all the material has experienced plastic strains in excess of 100%. It is therefore reasonable to conclude that bulge failure (target perforation) would have occurred no later than 250 to 275 μs.

The final ratio of residual velocity to impacting velocity (V_r / V) is 0.74. If failure would have occurred at 250 μs, then V_r / V—using conservation of momentum and the fact that the velocity decreases linearly from the penetration velocity to the tail velocity over a distance of two projectile diameters [6]—would have been approximately 0.85, which is in excellent agreement (0.86) with the results of Fig. 79 from Ref. [10] (using a value of 0.58 for the plate thickness normalized by the projectile length, i.e., $T/L = 0.58$).

The nose and tail velocities of the projectile differ by 120 m/s at breakout (see Fig. 11). We can calculate how long it should take for the projectile velocity to equilibrate. One elastic wave transit changes the velocity by 47 m/s [$\Delta u = 2\sigma_p / (\rho_p s_p)$ where σ_p, ρ_p, and s_p are the flow stress, density, and longitudinal wave speed, respectively, of the tungsten projectile; the dynamic flow stress for the tungsten alloy is approximately 2 GPa, ρ_p is 17.2 g/cm^3, and s_p is 4900 m/s]. Thus, it requires 2.5 wave transits for the projectile velocity to equilibrate. We can estimate the length of the projectile at breakout from Fig. 12, the projectile is approximately 12 cm long. Thus, it will take 61 μs to equilibrate. If the time of breakout is approximately 335 μs, then equilibration will occur at 396 μs, in excellent agreement with the results in Fig. 8. The normalized residual length (L_r / L) is 0.39, which also is in good agreement (within 10%) with data from experiments by Hohler and Stilp [10].

Strain-Rate Dependent Modeling. The computational results for the two scale sizes were again compared with the strain-rate terms zeroed in Eqs. (1-2) to ascertain if there existed any numerical rate effects associated with target breakout and perforation. The numerical results were identical. Then the problems were rerun including the strain-rate term in the constitutive models. The one-tenth-scale results for the penetration and tail velocities are overlaid onto the graph with the full-scale results, Fig. 13. It is seen that the full-scale penetration velocity increases at a slightly higher rate than for the tenth-scale projectile. The residual velocity, after target perforation, of the prototype projectile is approximately 5% higher than for the model projectile.

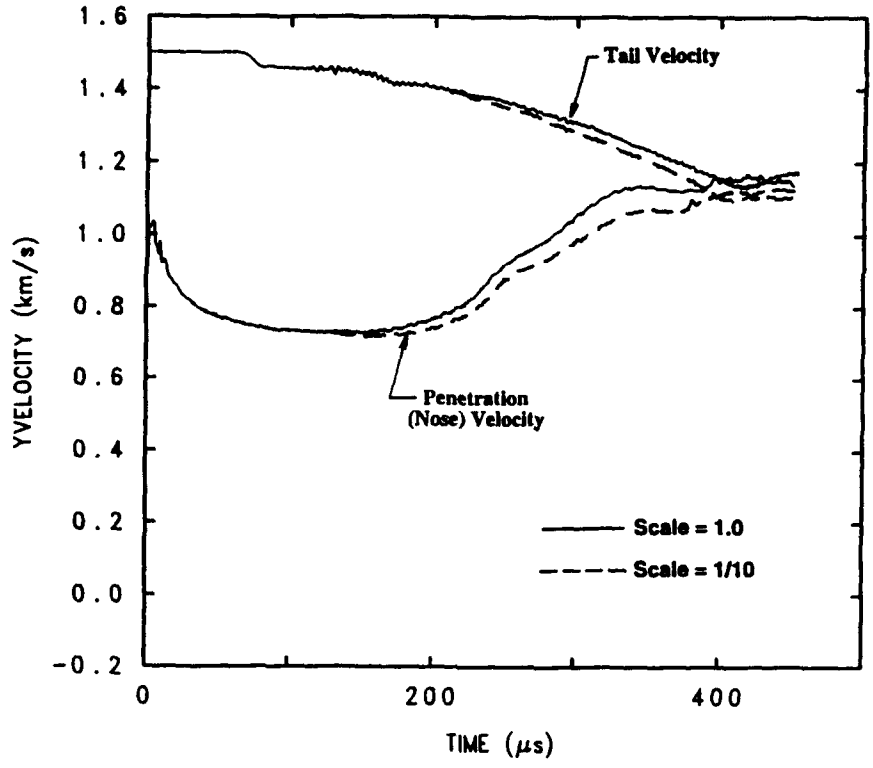

Figure 13. Centerline Penetration and Tail Velocities versus Time: Finite-Thickness Targets

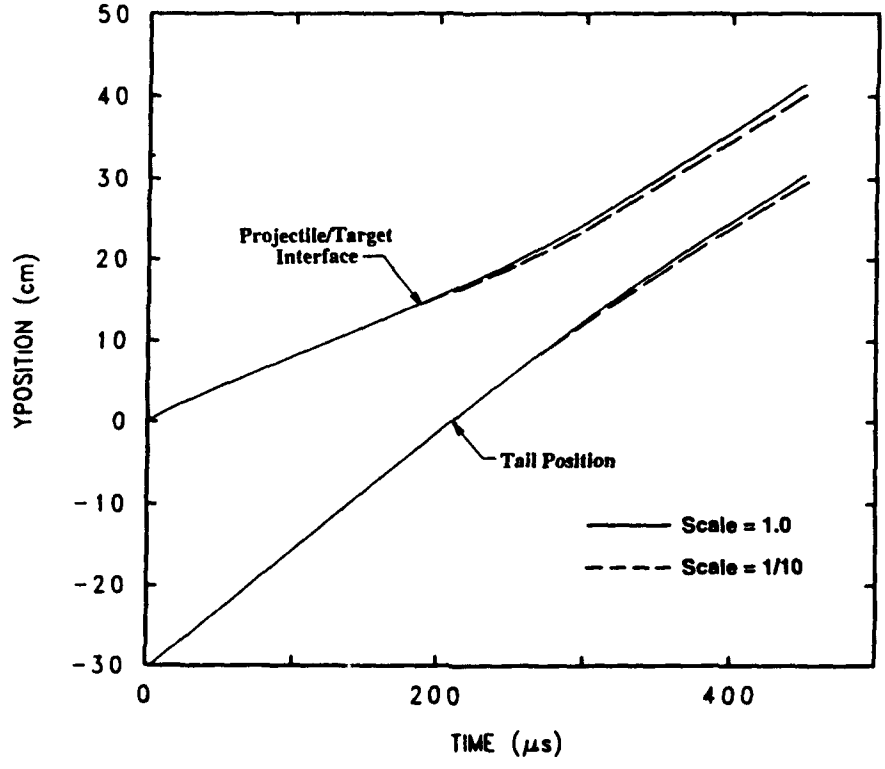

Figure 14. Centerline Penetration (Interface) and Tail Positions versus Time: Finite-Thickness Targets

The positions versus time of the nose and tail for prototype and model projectiles are shown in Fig. 14. At homologous times, the scaled projectile has not gone as deep as the prototype projectile. Thus, a conclusion similar to that for the semi-infinite target is reached: the scaled target is slightly "stronger." The normalized length of the projectiles L_f/L after perforation is 0.37 versus 0.35 for the prototype and model projectiles, respectively. Thus, the model projectile is approximately 5% shorter after perforation.

Damage Issues. There is an issue that has only been addressed obliquely at this point, however, and that is the issue of failure. Failure is known to grow with applied stress and time [11]. For example, the Tuler-Butcher model for spall failure [12] was developed to account for the observed dependence of spall failure on stress pulse duration. Failure is assumed to occur instantaneously when a critical value of the damage parameter K is reached:

$$K = \int_0^t (\sigma - \sigma_o)^\zeta dt \tag{4}$$

where σ is the tensile stress pulse of arbitrary shape, and σ_o is a threshold stress level below which no significant damage will occur regardless of stress duration. The material constant ζ is used to fit experimental data. More complicated models would also account for material degradation due to partial damage, e.g., the Cochran-Banner model [13].

Equation (4) was formulated specifically to model spallation numerically. The above argument concerning the effects of scale size and damage is strengthened further by examining nucleation and growth damage models. In particular, it is instructive to examine the work of Curran, et al. [14], since their work was largely motivated by a desire to develop computational damage models where the origins of the models are rooted in microscopic damage mechanics. Specifically, we will discuss ductile fracture that results from the nucleation, growth, and coalescence of voids. In their model, damage increases by nucleation of new voids and by growth of existing voids. The rate at which the number of voids is nucleated, $\dot{N}$, is governed by the tensile overstress in the solid material (not the average pressure in the composite of solid and voids):

$$\dot{N} = \begin{cases} \dot{N}_o \exp[(P_s - P_{th0})/P_1] & P_s > P_{th0} \\ 0 & P_s \le P_{th0} \end{cases} \tag{5}$$

where P_s is the tensile stress in the solid and P_{th0} is a threshold tensile stress for nucleation of voids; $\dot{N}_o$, P_{th0} and P_1 are material constants. In a time step Δt, the void volume, ΔV_n, nucleated is proportional to $\dot{N}\Delta t$. Under high rates of loading, inertial and viscous effects dominate the growth of voids, and it can be shown that the void volume, V_v, also grows according to a tensile overstress:

$$V_v = V_{vo}\exp\left(3\frac{P_s - P_{th1}}{4\eta}\Delta t\right) \tag{6}$$

with V_{vo} being the void volume at the beginning of a time interval, P_{th1} is a tensile threshold stress for void growth, and η is a material viscosity. Thus, the total void volume at the end of each time step Δt is given by:

$$V_v = V_{vo}\exp\left(3\frac{P_s - P_{th1}}{4\eta}\Delta t\right) + \Delta V_n \tag{7}$$

Damage development has a strong dependence on time: nucleation of voids depends linearly on time, and the growth of voids increases exponentially with time.

Time scales as $1/\lambda$. The stresses, to first order (aside from strain-rate effects), are the same at the two scales. Therefore, both Eq. (4) and Eqs. (5-7) indicate that the damage will not be the same at homologous times. Assuming that the same value of K [from Eq. (4)] or V_v [from Eq. (7)] is required for failure in the model and prototype, then the smaller scale will have less damage than the larger scale at homologous times (due to less absolute time transpiring in the model). In this sense, the smaller scale "appears" stronger.

There is a caveat to the above argument, however. If the stress is far above damage thresholds, the damage rate is quickly saturated, and the time-evolution model can be replaced by a much more simplistic "sudden damage" criterion. An appropriate critical level can be estimated from known material properties, e.g., total equivalent plastic strain at failure. Reference [15] discusses computational failure models, and provides an example that demonstrates that computational results are insensitive to the details of failure when a projectile overmatches a target. If a maximum stress, equivalent plastic strain, or plastic work is a suitable failure criterion, then there will be no differences in failure between the model and prototype (per the model law of Table 4), except for slight differences in the stress resulting from strain rate.

We thus conclude that differences in damage between a model and prototype can result from two factors: 1) near thresholds, damage growth is time-dependent, and since time scales as the inverse of the scale factor, less damage will accumulate in a smaller model at homologous times; and 2) strain-rate effects will increase the strength of the material, which again will be most noticeable near damage thresholds. If the target is overmatched, damage is insensitive to the value of the damage parameter (e.g., critical equivalent plastic strain). Therefore, if the target is overmatched, there should be little scale dependence (our study indicates about 5%). Near thresholds, smaller targets will appear stronger because strain-rate effects increase the strength of the material and because the same degree of damage has not developed at homologous times.

4.0 SUMMARY

We have examined the penetration and perforation of semi-infinite and finite-thickness targets. Numerical simulations have been used to quantify the distortion in penetrator and target response due to higher material flow stresses that result from the higher strain rates at smaller scales. We have shown that target resistance is sightly greater for small scale targets due to strain-rate hardening. For the impact scenarios examined here, i.e., a tungsten long rod impacting an armor steel target at 1.5 km/s, we conclude that the magnitude of strain-rate effects, however, are difficult to separate from experimental scatter. Over a scale factor of ten, the increased target resistance results in normalized penetration being less by approximately 5% for semi-infinite targets; the residual velocity and normalized residual projectile length are approximately 5% less for a finite-thickness target. One aspect of target perforation not explicitly quantified, but discussed qualitatively, deals with failure. Near a limit condition, where the details of the time evolution of failure are important, damage will not be as severe in the scaled target as the prototype target because damage evolution is a function of absolute time and not the scale time. Therefore, a smaller scale will have less damage than the larger scale at homologous times. These effects probably can be observed in well-controlled experiments.

5.0 ACKNOWLEDGEMENTS

This work was performed under contract DAAL03-91-C-0021, funded by the Defense Advanced Projects Agency and administered by the U.S. Army Research Office. The authors wish to thank Dr. James D. Walker for his suggestions during the course of this study, and we would like to acknowledge the support and encouragement of Dr. Peter Kemmey at DARPA and Mr. René Larriva at Interferometrics, Inc.

6.0 REFERENCES

1. C. C. Lin and L. A. Segel, ***Mathematics Applied to Deterministic Problems in the Natural Sciences***, Macmillan Publishing Co., Inc., NY, 1974.

2. J. M. McGlaun, S. L. Thompson, and M. G. Elrick, "CTH: A Three-Dimensional Shock Wave Physics Code," *Int. J. Impact Engng*, **10**, pp. 351-360 (1990).

3. W. W. Predebon, C. E. Anderson, Jr., and J. D. Walker, "Inclusion of Evolutionary Damage Measures in Eulerian Wavecodes," *Computational Mechanics*, **7**(4), pp. 221-236 (1991).

4. S. A. Silling, "Stability and Accuracy of Differencing Schemes for Viscoplastic Models in Wavecodes," SAND91-0141, Sandia National Laboratories, Albuquerque, NM (1991).

5. G. R. Johnson and W. H. Cook, "Fracture Characteristics of Three Metals Subjected to Various Strains, Stain Rates, Temperatures and Pressures," *Engineering Fracture Mechanics*, **21**(1), pp. 31-48 (1985).

6. C. E. Anderson, Jr. and J. D. Walker, "An Examination of Long-Rod Penetration," *Int. J. Impact Engng.*, **11**(4), pp. 481-501 (1991).

7. C. E. Anderson, Jr., "An Overview of the Theory of Hydrocodes," *Int. J. Impact Engng.*, **4**(1-4), pp. 35-59 (1987).

8. C. E. Anderson, Jr., J. D. Walker, and G. E. Hauver, "Target Resistance for Long-Rod Penetration into Semi-Infinite Targets," Post-SMIRT Seminar Impact III, The University of Tokyo, Tokyo, Japan, August 26-28 (1991).

9. M. Ravid and S. R. Bodner, "Dynamic Perforation of Viscoplastic Plates by Rigid Projectiles," *Int. J. Engng. Sci.*, **21**(6), pp. 577-591 (1983).

10. V. Hohler and A. J. Stilp, "Long-Rod Penetration Mechanics," in ***High Velocity Impact Dynamics***, J. A. Zukas (ed), John Wiley & Sons, NY, pp. 394-395 (1990).

11. J. A. Zukas, T. Nicholas, H. G. Swift, L. B. Greszczuk, and D. R. Curran, ***Impact Dynamics***, John Wiley & Sons, Inc., pg. 408 (1982).

12. F. R. Tuler and B. M. Butcher, "A Criterion for the Time Dependence of Dynamic Fracture," *Int. J. Fract. Mech.*, **4**(4), pp. 431-437 (1968).

13. S. Cochran and D. Banner, "Spall Studies in Uranium," *J. Appl. Phys.*, **48**(7), pp. 2729-2737 (1977).

14. D. R. Curran, L. Seaman, and D. A. Shockey, "Dynamic Failure of Solids," *Physics Reports (Review Section of Physics Letters)*, **147**(5 & 6), pp. 253-388 (1987).

15. C. E. Anderson, Jr. and S. R. Bodner, "Ballistic Impact: The Status of Analytical and Numerical Modeling," *Int. J. Impact Engng.*, **7**(1), pp. 9-35 (1988).